

Imaging of Vascular Chaos

Randall L. Barbour¹ Harry L. Graber¹, Yaling Pei², and Christoph H. Schmitz¹

1. SUNY Downstate Medical Center, 450 Clarkson Avenue, Brooklyn, NY 11203
2. NIRx Medical Technologies Corp., 15 Cherry Lane, Glen Head, NY 11545

ABSTRACT

Dynamic processes in biology are often controlled by multiple parameters that interact in a complex nonlinear fashion. Increasingly, evidence has accumulated that such behavior exhibits the property of sensitivity to initial conditions, a feature exhibited by chaotic systems. One such system is the vasculature. In this report, we present what we believe is the first experimental demonstration ever of imaging chaotic behavior of the vasculature in a large tissue structure (*i.e.*, the human forearm). Supporting these findings are results from numerical simulation demonstrating our ability to image and correctly characterize complex dynamic behavior in dense scattering media that experience spatiotemporally coincident variations in hemodynamic states.

Keywords: Dynamic optical tomography, Physiological dynamics, Physiological oscillations, Inverse problem.

1. INTRODUCTION

In a series of accompanying reports we describe instrumentation¹ and numerical methods² that we have developed for the collection and analysis of time-series image data. These capabilities represent various components of a more inclusive methodology that we seek to apply for the characterization of the spatiotemporal properties of vascular reactivity in large tissues using near infrared optical imaging methods. It is our belief that such measures performed on tissue, either at rest or in response to homeostatic provocation, represents a large untapped reservoir for identifying new diagnostic measures of disease processes, as well as for monitoring the influence of a host of therapeutic regimens.

Studies of dynamic processes in biology have indicated that the form of the function governing a process can have important implications for the approaches taken in detecting early-stage disease processes and for devising new therapeutic strategies. Central to this concept is the recognition that natural systems tend to organize themselves in ways that retain maximal flexibility while expending minimal energy. These are properties common to systems whose dynamics are governed by chaotic nonlinear processes. While the term “chaos” suggests unbridled disorganization in common parlance, here it refers to a more constrained state wherein, although some elements of randomness exist, the system is nevertheless governed by deterministic processes that interact in a nonlinear fashion, that have the property of sensitive dependence on initial conditions.³

Increasingly, evidence is accumulating that this property both is pervasive in biology and has important implications for clinical medicine. For instance, a common goal in therapeutics is to restore normal body function by achieving some steady-state concentration of a drug until clinical symptoms subside. While experience has taught us that the approach does work, not infrequently the range of success is quite large and includes a disturbing fraction of individuals for whom the treatment is notably ineffective. One consequence of chaotic behavior in physiological systems is the introduction of a temporal component into the consideration of therapeutic strategies. Thus it is not just deciding which drug and how much to give, but the timing of dosages as well, that can be relevant.

A working hypothesis we have adopted is that improved therapeutic outcomes might be achieved if detailed information regarding the dynamics of the vascular response were available. Given the central role of the vasculature in drug and nutrient delivery, gas exchange, and serving as a conduit for local and distant effectors, we believe the availability of a noninvasive, continuous, real-time imaging technology sensitive to vascular dynamics may prove useful in devising improved dosing schedules.

As noted in accompanying manuscripts,^{1,2,4,5} we believe the method of dynamic optical tomography is well suited for monitoring vascular dynamics. In this report we have explored this potential by imaging and quantifying dynamics of vascular reactivity in the human forearm in response to a periodic respiratory stimulus. The acquired image time series was then subjected to an analysis in which parameters whose values suggest the occurrence of chaotic nonlinear behavior were

quantified. Results obtained strongly indicate that such behavior, previously reported to occur in near surface microvessels,⁶ is observable in cross-section. As further evidence of the fidelity of the methodology, we have characterized the ability to reliably extract detailed measures of simulated complex dynamics occurring in localized regions within a dense scattering medium.

2. METHODS

2.1 Data collection for forearm and laboratory phantom studies

Time series of tomographic data from a human forearm were collected while the volunteer followed a controlled-respiration protocol. The influence of a respiratory stimulus was chosen as a simple noninvasive means to amplify the natural oscillatory activity of the vasculature. The respiration rate was 0.08 Hz for the first 150 time points, and then was increased to 0.16 Hz for the remainder of the measurement period. To assist in timing and repeatability, the volunteer was asked to adjust his respiratory rate to match the beat frequency of a metronome. A total of 240 sets of tomographic measurements (6 sources, 18 detectors) were collected, at a rate of 2.8 Hz. Detector data were collected using a recently described measuring system.⁷ The measuring head used contained eighteen optical fiber bundles uniformly spaced in a circular array. At each of six uniformly spaced illumination sites, light from a laser diode operating at 810 nm was directed to the tissue. The optical power delivered to the tissue surface was approximately 5 mW.

Time series imaging data was also collected under the same conditions as the forearm studies from a static laboratory phantom composed of white Delrin[®]. The phantom was cylindrical in shape with a diameter of 9 cm and a height of 15 cm. This data was collected to serve as a control so as to distinguish stochastic data from the physiological findings.

2.2 Design of simulation study

The purpose of this study was to define the accuracy with which the methods used to analyze the experimental data can define complex time-varying hemodynamic processes occurring in highly scattering media. Simulated was a 2D structure containing two inclusions. Each inclusion was assigned different time varying levels in tissue blood volume (V_b) and blood oxygen saturation (sO_2) within a background having static levels of each parameter. Thus we considered a state where the hemodynamic parameters in the inclusions are varying independently from each other, yet both are spatially and temporally coincident. Figure 1 shows a sketch of the target medium studied. The values for (V_b) and (sO_2) for the background closely agree with the approximate average tissue oxygenation level and blood volume seen in breast tissue.⁸ The ranges assigned to the hemodynamic parameters and the types of temporal fluctuation modeled are specified in Table 1. The ranges indicated for V_b and sO_2 represent 20% fluctuations about mean values of 5% and 70%, respectively. Assigned to the left-hand inclusion was a quasiperiodic time series for $V_b(l,t)$ and a chaotic time series for $sO_2(l,t)$. The former was generated by adding two sinusoidal functions whose frequency ratio was an irrational number,⁹ then computing one thousand function values at regular spaced time intervals. A chaotic time series was generated by assigning randomly generated initial values to the Hénon equation,¹⁰ and then iterating the equation one thousand times. Assigned to the right-hand inclusion was a chaotic time series for $V_b(r,t)$ and a stochastic time series for $sO_2(r,t)$. Note that while solutions to the Hénon equation were used to simulate dynamic behavior in both inclusions, by choosing different initial values, the chaotic time series generated are uncorrelated. The stochastic time series was generated by drawing one thousand independent samples from a random variable uniformly distributed between -1 and +1.

Figure 1 Dimensions and geometry of target medium

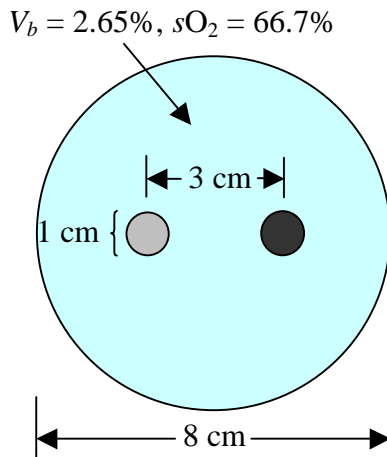


Figure 2 shows scaled plots of the first two hundred points (out of 1000) of the four assigned aperiodic functions. Note that the particular forms of the functions chosen were not in any way meant to reflect actual changes occurring *in vivo*. Instead they were chosen to simply represent examples of complex behaviors in that can occur in hemodynamic states. As a general tissue model, we are aware that it does not account for the expected contributions from myoglobin or other heme proteins. We have not specifically included corresponding variability in myoglobin in our model, as its level is nearly constant in tissue¹¹ and it has been previously suggested that its oxygenation state¹² is mainly time-invariant.

To *image* the temporal variability in the assigned *hemodynamic* properties it was necessary to simulate a two-wavelength measurement, then compute an image time series of the absorption coefficient at each wavelength, and derive from these independent solutions estimates of the assigned hemodynamic parameters. This was performed by computing optical absorption coefficient values that correspond to the known optical properties of hemoglobin at 760 nm and 840 nm, and to the assigned value for (V_b) and (sO_2), using the formula

$$\mu_{amed}^{\lambda}(t) = V_b(t) \{ sO_2(t) \mu_{aoxy}^{\lambda} + [1 - sO_2(t)] \mu_{ared}^{\lambda} \}. \quad (1)$$

The value computed for $\mu_{amed}^{\lambda}(t)$ (cm^{-1}) is the medium absorption coefficient, at wavelength λ , that corresponds to the designated oxygen saturation level and blood volume, while μ_{aoxy}^{λ} and μ_{ared}^{λ} are the (time-independent) absorption coefficients (cm^{-1}) of the oxygenated and reduced forms, respectively, of tetrameric Hb at wavelength λ . (The Hb absorption coefficients were, in turn, computed via the formula $\mu_{ax}^{\lambda} = 4000c\epsilon_x^{\lambda}/M$, where ϵ_x^{λ} is the monomeric millimolar extinction coefficient¹³ (dimensions are $cm^{-1} mM^{-1}$) of Hb at wavelength λ and in oxygenation state x (*i.e.*, $x = \text{'oxy'}$, 'red'), M is the molecular weight of Hb, and c is its concentration. The numerical values used were $M = 64,500 \text{ g mol}^{-1}$ and $c = 150 \text{ g L}^{-1}$.)

Table 1 Temporal fluctuations in hemodynamic properties of inclusions

V_b			sO_2		
Range (%)	Dynamics		Range (%)	Dynamics	
	Left	Right		Left	Right
4 – 6	Quasiperiodic	Chaotic	56 – 84	Chaotic	Stochastic

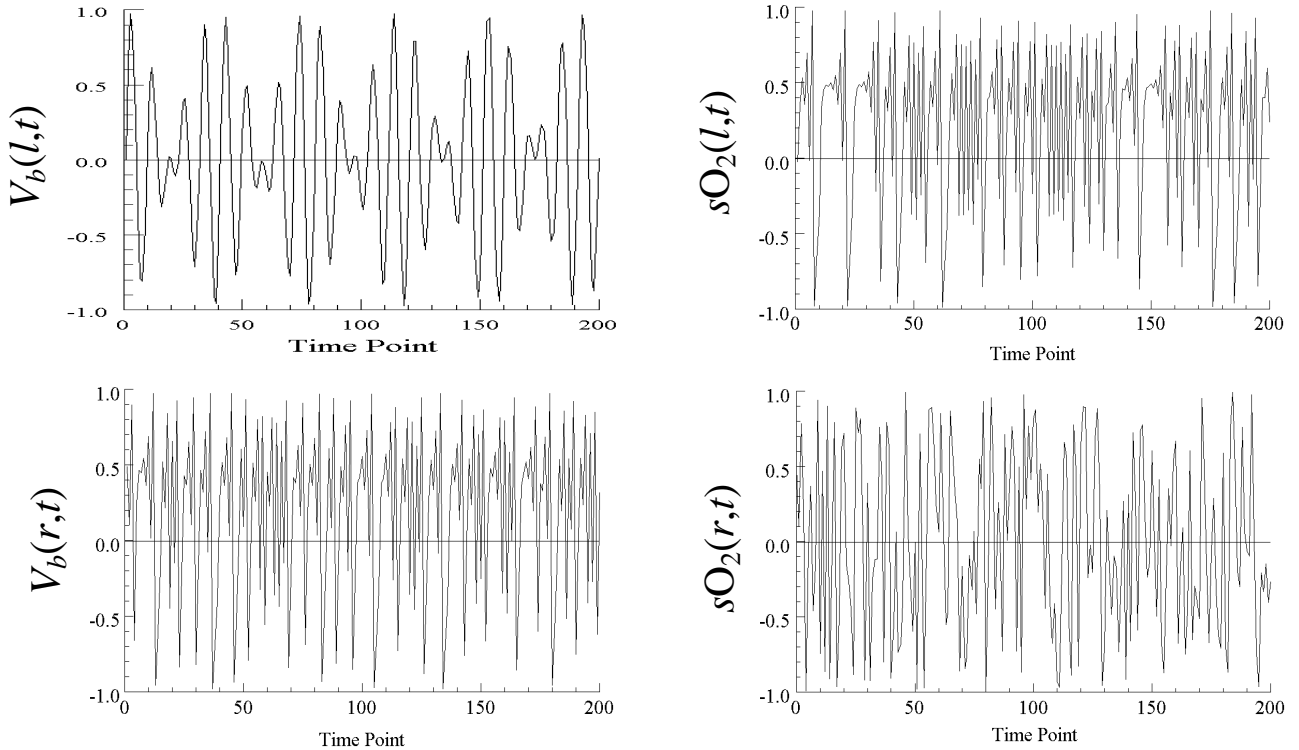


Figure 2 Plots of initial 200 time points, out of 1000 simulated values, of modeled functions assigned to the indicated hemodynamic parameters in the target medium's inclusions. Note that the plotted functions have been rescaled to range from -1 to $+1$.

Note that the reduced scattering cross section (μ_s') in the medium, while spatially varying (10 cm^{-1} in the background and 15 cm^{-1} in both inclusions), was temporally static throughout the medium.

2.3 Forward Modeling

Tomographic data for the simulated tissue models were acquired by using the finite–element method to solve the diffusion equation for a DC source, with extended Dirichlet boundary conditions.^{2,14} For a spatial domain Λ with boundary $\partial\Lambda$, this is represented by the expression

$$\nabla \cdot [D(\mathbf{r})\nabla\phi(\mathbf{r})] - \mu_a(\mathbf{r})\phi(\mathbf{r}) = -\delta(\mathbf{r} - \mathbf{r}_s), \quad \mathbf{r} \in \Lambda, \quad (2)$$

where $\phi(\mathbf{r})$ is the photon intensity at position \mathbf{r} , \mathbf{r}_s is the position of the DC point source, and $D(\mathbf{r})$ and $\mu_a(\mathbf{r})$ are the position–dependent diffusion and absorption coefficients, respectively. Here the definition used for the diffusion coefficient was $D(\mathbf{r}) = 1/\{3[\mu_a(\mathbf{r}) + \mu_s'(\mathbf{r})]\}$, where $\mu_s'(\mathbf{r})$ is the position–dependent reduced scattering coefficient. Forward–problem solutions were computed for each of six sources positioned about the target at 60° intervals, with each source located at a depth of 2 mm in from the extended boundary (*i.e.*, within the strip lying between the physical and extended boundaries).¹⁴ Intensity values at eighteen locations, at the same depth as the sources but spaced at 20° intervals, were used as detector readings. Imaging operators were computed, in the manner described in Ref. 2, for each of the resulting 108 source/detector pairs. Tomographic data sets of detector readings were computed for each of the time–varying optical coefficients (1000 total) assigned to the target inclusions. A single set of imaging operators, computed for a 8–cm–diameter homogeneous medium whose properties are equal to those of the static region of the target, was used for all inverse problem computations.

2.4 Image reconstruction methods

The optical inverse formulation was based on the normalized difference method,² in which the equation that we solve has the form

$$\mathbf{W}_r \delta \mathbf{x} = \delta \mathbf{I}_r, \quad (3)$$

where $\delta \mathbf{x}$ is the vector of differences between the optical properties (*e.g.*, absorption and scattering coefficients) of a target (measured) and a “background” medium, \mathbf{W}_r is the weight matrix describing the influence that each voxel or element has on the surface detectors for the selected reference medium, and $\delta \mathbf{I}_r$ represents a modified difference between detector readings obtained from the target in two distinct states. The normalized difference is defined by

$$(\delta \mathbf{I}_r)_i = \frac{(\mathbf{I} - \mathbf{I}_0)_i}{(\mathbf{I}_0)_i} (\mathbf{I}_r)_i, \quad (4)$$

where \mathbf{I}_r is the computed detector readings corresponding to a selected reference medium, and \mathbf{I} and \mathbf{I}_0 represent two sets of measured data (*e.g.*, background *vs.* target, time–averaged mean *vs.* a specific time point, prior and subsequent to an evoked response, *etc.*).

For both the simulation and experimental laboratory data, image reconstructions were carried out by using a conjugate gradient descent (CGD) algorithm to compute numerical solutions to the modified perturbation equation, without imposition of any constraints or weight–matrix scaling.

2.4.1 Simulation Study

Spatial maps of the assigned hemodynamic parameters for the simulated 2D medium were computed by combining the reconstruction results obtained from the independent computations of optical properties corresponding to simulated measurements performed at 760 and 840 nm, according to Eq. (5).

Note that the reconstruction algorithm did not consider any interaction between the detector data at the two wavelengths, nor any *a priori* knowledge that the medium’s μ_s' and background μ_a were static. Thus two independent sets of reconstructions were performed, of $\mu_{amed}^{760}(t)$ and $D_{med}^{760}(t)$ in the one case, and of $\mu_{amed}^{840}(t)$ and $D_{med}^{840}(t)$ in the other. The hemodynamic parameters were subsequently derived from the reconstructed $\mu_{amed}^{760}(t)$ and $\mu_{amed}^{840}(t)$, via the formulas

$$V_b(t) = \frac{(\mu_{a\text{red}}^{840} - \mu_{a\text{oxy}}^{840})\mu_{a\text{tis}}^{760}(t) - (\mu_{a\text{red}}^{760} - \mu_{a\text{oxy}}^{760})\mu_{a\text{tis}}^{840}(t)}{\mu_{a\text{red}}^{840}\mu_{a\text{oxy}}^{760} - \mu_{a\text{red}}^{760}\mu_{a\text{oxy}}^{840}}, \quad (5)$$

$$S_{\text{O}_2}(t) = \frac{\mu_{a\text{red}}^{840}\mu_{a\text{tis}}^{760}(t) - \mu_{a\text{red}}^{760}\mu_{a\text{tis}}^{840}(t)}{(\mu_{a\text{red}}^{840} - \mu_{a\text{oxy}}^{840})\mu_{a\text{tis}}^{760}(t) - (\mu_{a\text{red}}^{760} - \mu_{a\text{oxy}}^{760})\mu_{a\text{tis}}^{840}(t)},$$

which we get by inverting the two–equations–in–two–unknowns system obtained from Eq. (1), with one equation explicitly for $\lambda = 760$ nm and the other explicitly for $\lambda = 840$ nm.

2.4.2 Forearm and laboratory phantom studies

Optical measurements of the forearm and static phantom were performed at 810 nm. Use of only one wavelength, restricts the ability to simultaneously deduce tissue blood volume and blood oxygen saturation from the reconstructed absorption coefficients. The 810 nm light that was employed does, however, lie near an isosbestic point in the Hb absorption spectrum.¹³ Therefore, in the case of forearm image time series, fluctuations in the reconstructed μ_a time series can be interpreted as reflective of temporal variability in V_b (while any seen in the Delrin[®]–rod image time series is indicative of random noise). The time–series analysis operations described below accordingly were carried out directly on the reconstructed $\mu_a(t)$ for these cases. Prior to performing these computations, the μ_a time series for each image pixel was band–pass filtered over a range that included the vasomotor and respiratory frequencies (0.05–0.35 Hz).

2.5 Post–reconstruction image analysis

Two measures of interest of spatiotemporal data sets are (1) an estimate of the accuracy with which temporal behavior is recovered and spatially mapped, and (2) insight regarding the origin of the temporal behavior itself. Measures of the first provide an assessment of the fidelity of the applied technology. The second seeks to understand the biological basis for the behavior. To characterize these we have adopted a three–fold analysis scheme. For the latter we have computed two measures that reflect the complexity of temporal behavior. For the former, we have introduced a test to determine the temporal accuracy of the recovered behavior, as well as a test to determine how accurately this behavior is spatially mapped.

2.5.1 Measures of Complexity

Measures of complexity can provide an understanding of the minimum number of interacting parameters and manner in which they interact. Two extensively studied statistics that convey this information are the *correlation dimension*¹⁵ (CD) and the *maximal Lyapunov exponent*¹⁶ (mLE) of a time series. These quantities are computed from *pseudo–state–space* (PSS) representations of the data in a time series. Briefly, a time series consisting of numbers x_1, x_2, \dots, x_n is “embedded” into a PSS of dimension m by re–sorting the x s into m –dimensional vectors $\mathbf{X}_1 = (x_1, x_{1+\tau}, \dots, x_{1+(m-1)\tau})$, $\mathbf{X}_2 = (x_2, x_{2+\tau}, \dots, x_{2+(m-1)\tau})$, *etc.*; the parameter τ that appears here is called the “time delay.” Selecting the “correct” values for m and τ in a given case remains something of an art, although useful guidelines have been given by Griffith,¹⁷ and a lower limit for m can be obtained by the “method of false nearest neighbors.”¹⁸

The CD of a time series is found by first computing the correlation *integral*,¹⁵

$$C(r) \equiv \sum_{i,j=1}^N \theta(r - |\mathbf{X}_i - \mathbf{X}_j|) / N^2, \quad (6)$$

where N is the number of data vectors, and $\theta(z)$ is the Heaviside function: $\theta(z) = 1$ if $z \geq 0$, $\theta(z) = 0$ if $z < 0$. The operation defined by Eq. (6) amounts to counting the number of vectors that lie within a distance r of each other, as a function of r . In the limit as r approaches zero, invariably it is found that

$$C(r) \propto r^\nu \quad (7)$$

for some positive real ν . The specific value of ν obtained for a given time series is its CD.¹⁵

The CD is interpretable as a lower limit on the number of variables that must be present in the dynamical system that gave rise to a time series. If the x s are generated by a deterministic dynamical system, it is found that with increasing m , the computed CD eventually saturates, *i.e.*, reaches a finite limiting value, while the CD computed for a truly stochastic time

series increases indefinitely with increasing m . In addition, in those cases in which the dynamics are predictable (*i.e.*, periodic, which necessarily includes all linear dynamical systems), the CD will be an integer, while a fractional CD indicates that the time series defines a fractal structure in the PSS, which in turn implies that the dynamics are nonlinear,¹⁷ and in many cases — although, as Ditto *et al.* have shown,¹⁹ not always — chaotic.

Computation of maximal Lyapunov exponent

In general, a time series embedded in a m -dimensional PSS will have m Lyapunov exponents $\lambda_1, \dots, \lambda_m$. (Thus if the value chosen for m is larger than needed to obtain an accurate ν , some of the λ s will be spurious; however, methods for identifying these are available.²⁰) Their significance is most easily grasped by imagining an infinitesimally small sphere centered about an arbitrarily chosen point in the PSS, and supposing that every point within the sphere represents the initial vector of a time series, all generated by the same dynamical process but with slightly different initial conditions. Then, the vectors representing the future states of the system at any given future moment will fill not a sphere, but an ellipsoid. This ellipsoid will have m principal axes, each of whose lengths is time-varying: $\varepsilon_1(t), \varepsilon_2(t), \dots, \varepsilon_m(t)$.²¹ It happens that each axis length varies approximately exponentially in time,

$$\varepsilon_i(t) \approx \varepsilon_i(0)e^{\lambda_i t}, \quad (8)$$

and λ_i is, by definition, the i^{th} Lyapunov exponent.²¹ While the *sum* of all λ s must be negative if the dynamic system under consideration is dissipative, one or more of the individual λ s may be positive. The presence of even one positive Lyapunov exponent is diagnostic of chaotic dynamics, as it implies that two time series that begin arbitrarily close together will become increasingly different from each other with the passage of time (*i.e.*, the system exhibits *sensitive dependence on initial conditions*³).

As in most other practical applications to date, for this report we have focused on computing estimates of the largest exponent, λ_1 , and typically are more concerned with knowing its algebraic sign than its specific value, as this is the feature that distinguishes between chaotic and non-chaotic dynamics. The method we use for calculating λ_1 was developed by Rosenstein *et al.*¹⁶ In common with the algorithm for estimating the CD, the first step consists of identifying all inter-vector distances $d_j(i)$ in the PSS, where here i is the time index and j is the vector-pair index. Then the quantity

$$y(i) \equiv \langle \ln d_j(i) \rangle / \Delta t \quad (9)$$

is calculated, where the indicated averaging is performed over all values of j , and Δt is the interval between points in the time series. Finally, λ_1 is estimated as the slope of the best-fitting line obtained by linear regression of $y(i)$ vs. i .¹⁶

2.5.2 Assessment of temporal accuracy

PSS plots provide a simple means to detect patterns and regularities in, and constraints on, the reconstructed system behavior that are not evident from direct inspection of the time-series functions themselves. Here we have used this method to provide a graphical means to judge the accuracy of the recovered temporal behavior in the two recovered hemodynamic parameters.

2.5.3 *Quantitative assessment of spatial localization of dynamic behavior.* Estimates of the spatial accuracy of recovered temporal behavior was judged by generating maps of the covariance (σ_{xy}) between the derived $V_b(t)$ and $sO_2(t)$ in every pixel and each of the functions $V_b(l,t)$, $sO_2(l,t)$, $V_b(r,t)$, and $sO_2(r,t)$. Here a perfect reconstruction result would produce spatial maps for which only one of the modeled hemodynamic parameters significantly co-varies with the corresponding modeled function. This measure was also used to examine the level of cross-talk between the two recovered parameters.

3. RESULTS

3.1 Forearm and laboratory phantom studies

As noted in the Introduction, the occurrence of chaotic nonlinear behavior may have important implications for disease diagnosis and approaches to therapy. Because of our ability to generate time-series image data, we have explored whether evidence might be gained from analysis of such data that is consistent with previous reports, which were based on surface measures, indicating that the vascular response may be governed by chaotic nonlinear processes.⁶ To examine this we have computed two measures, the correlation dimension (CD), and the maximum Lyapunov exponent (mLE) from pixel data obtained from the reconstructed image time series. These results are shown in Figures 3 and 4. Inspection of the color scale in Figure 3(A) reveals that most pixels within the cross-sectional map of the forearm have computed CD values that are

between 2 and 4. We note with considerable interest that this range coincides well with previous estimates of the CD of the microvascular response obtained from surface measures.⁶

We are aware that determination of the correlation dimension of a time series can be a tricky business, especially with small data sets.²² One concern is the expected dependence of the CD on the embedding dimension m . In the case of a chaotic function, the value of the CD, ν , should approach a finite limit as m increases without bound. In other results (not shown), we have observed this behavior for most of the pixel data explored in the image map. In fact, the computed CD map shown was obtained using $m = 20$ for a time delay (τ) of 1. As a control, we have collected time-series tomographic data from a static phantom (9-cm diameter white Delrin rod) and subjected the resultant image series to the same analysis as reported in figure 3(A). Analysis of stochastic data leads to two anticipated results. The first is that the value of the CD should show no sign of approaching a limiting value as m increases. This was observed for essentially all pixel data for the static phantom. The second is that significantly greater values of the CD should be obtained for stochastic data when the same values of m and τ are applied as were used in the generation of the data presented in Figure 3(A). Inspection of Figure 3(B) shows that this is observed, with most pixels having $\nu > 4$.

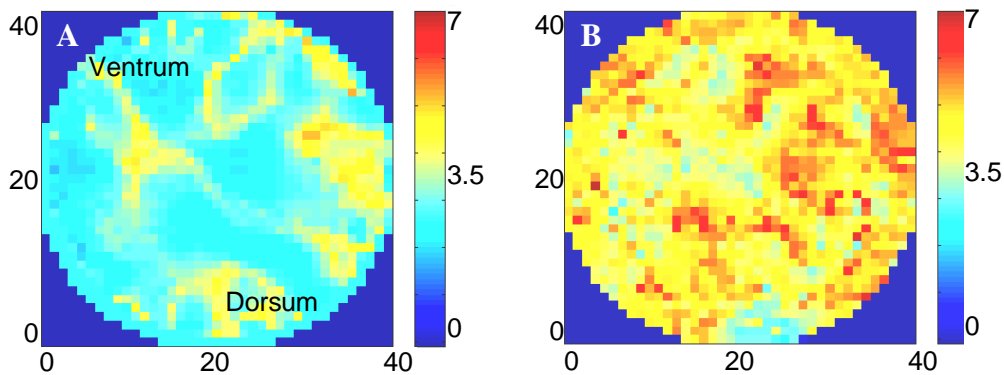


Figure 3 Correlation dimensions computed, in each pixel, from a time series of reconstructed images of μ_a (810 nm). (A), target medium is forearm of human volunteer; (B) target medium is a solid white Delrin[®] rod.

To further characterize the dynamics of the image pixel data we have computed corresponding spatial maps that reveal the mLE. This coefficient is a measure of the sensitivity to initial conditions. The value of the mLE is negative for systems experiencing converging behavior, zero for stochastic systems and positive for systems exhibiting chaotic behavior. Here again, we are aware that care must be exercised in analyzing small data sets.^{16,22} A control experiment often conducted to

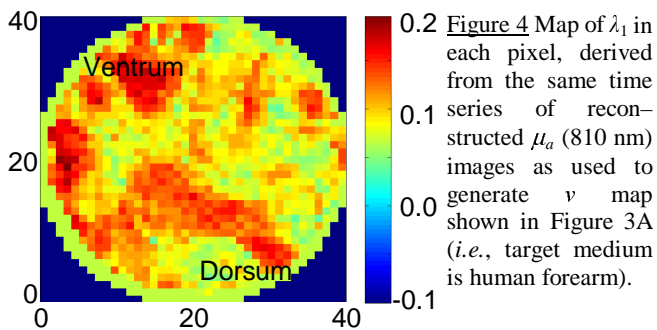


Figure 4 Map of λ_1 in each pixel, derived from the same time series of reconstructed μ_a (810 nm) images as used to generate ν map shown in Figure 3A (*i.e.*, target medium is human forearm).

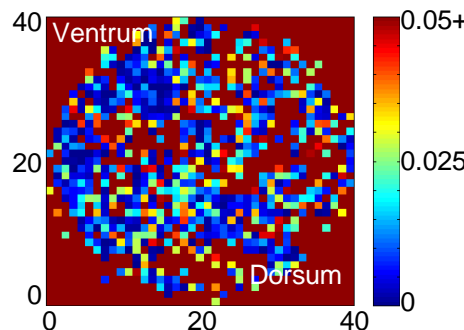


Figure 5 Comparison of λ_1 map in Figure 4 to corresponding results obtained from surrogate data sets. Number plotted in each pixel is the p-value (paired t-test, $n=5$) for the null hypothesis $\lambda_1 = \langle \lambda_1^{\text{sur}} \rangle$. Majority of pixels have p-values < 0.05 (*i.e.*, null hypothesis is rejected).

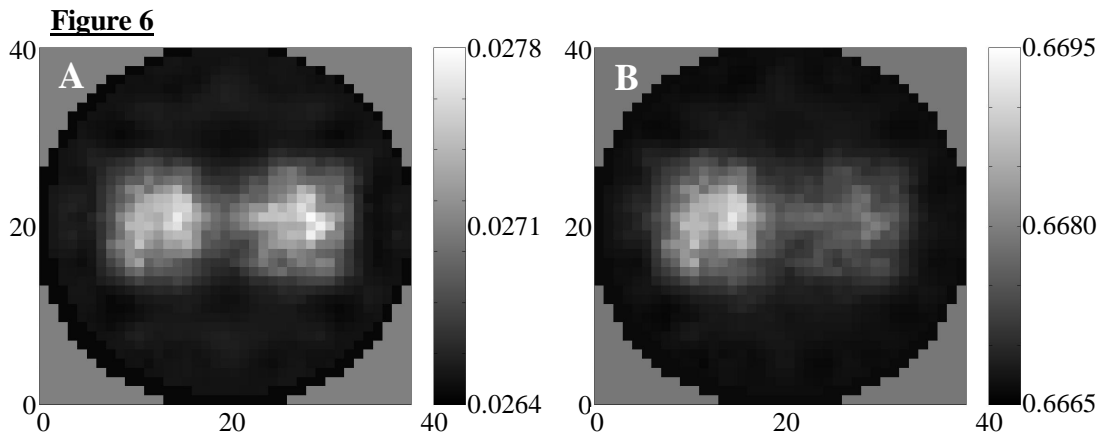
support evidence of chaotic behavior is to analyze surrogate data.²³ Surrogates are generated by randomizing the phase of a function's Fourier transform, computing the inverse Fourier transform, and deriving from the resulting function measures of the mLE. Typically, many such surrogates are computed to obtain statistical estimates of the similarity between the stochastic time series and the test time series. Figure 4 shows image maps that reveal the mLE for the physiological data set. The map shown in Figure 5 identifies the corresponding p-value for each pixel compared to pixel data generated from surrogate data. Inspection of Figure 4 reveals several areas in the cross section where the value for the mLE approaches 0.2. The image map in Figure 5 shows that these computed mLE values are, for most pixels, statistically different from those of

their surrogates, suggesting that the time series associated with most pixels is indeed chaotic. Thus we have identified two measures from the image pixel data that support the existence of chaotic behavior in the vascular response.

3.2 Simulation study

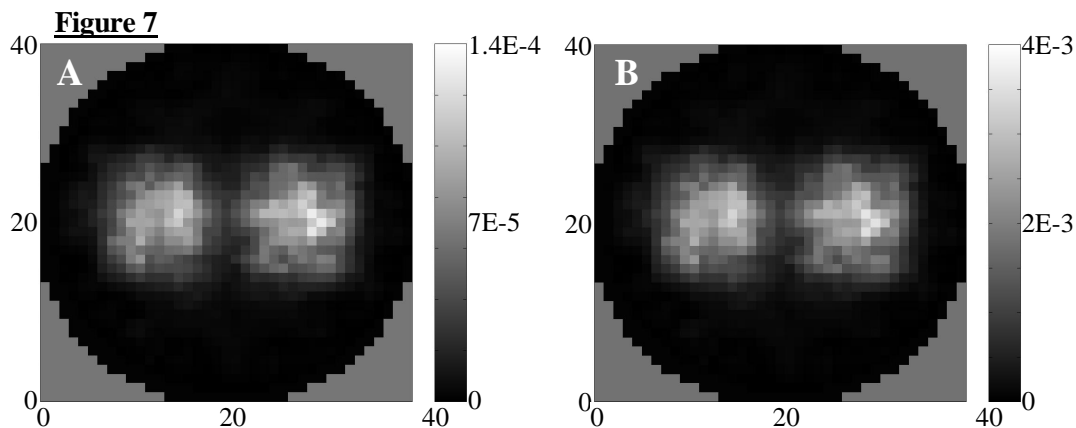
In an effort to gain further confidence in the reliability of the measures identified from the physiological time series image data, we have sought to characterize the accuracy by which these methods can correctly recover spatially distributed complex temporal behavior from simulated data. As an added measure of fidelity, these were applied to characterize spatiotemporal coincident behavior involving *hemoglobin states* whose coefficient values were derived from analysis of the two independent reconstructed image time series.

In Figure 6 we show a spatial map of the temporal mean value for $\langle V_b \rangle$ and $\langle sO_2 \rangle$ from the reconstructed image time series. Inspection shows that while the presence of two objects is apparent, their true sizes are overestimated, and they are not completely separated. In addition, the recovered parameter contrast is significantly underestimated. The true contrast of the inclusions relative to the background was 89% for $\langle V_b \rangle$ and 4.5% for $\langle sO_2 \rangle$. The corresponding values obtained from the reconstructed images were on the order of 10% of this value reflecting, in part, the influence of spatial blurring. We show this data to make the point, as we have recently reported,^{7,24-26} that whereas the quality of *time averaged* spatial maps is only fair, as will be shown, the quality of the temporal information derivable from an image time series can be much greater. As we have argued, this property reflects an intrinsic difference in the robustness of temporal measures.



Legend Time averaged image map of V_b (Panel A) and of sO_2 (Panel B) of the dynamic target medium sketched in Figure 1.

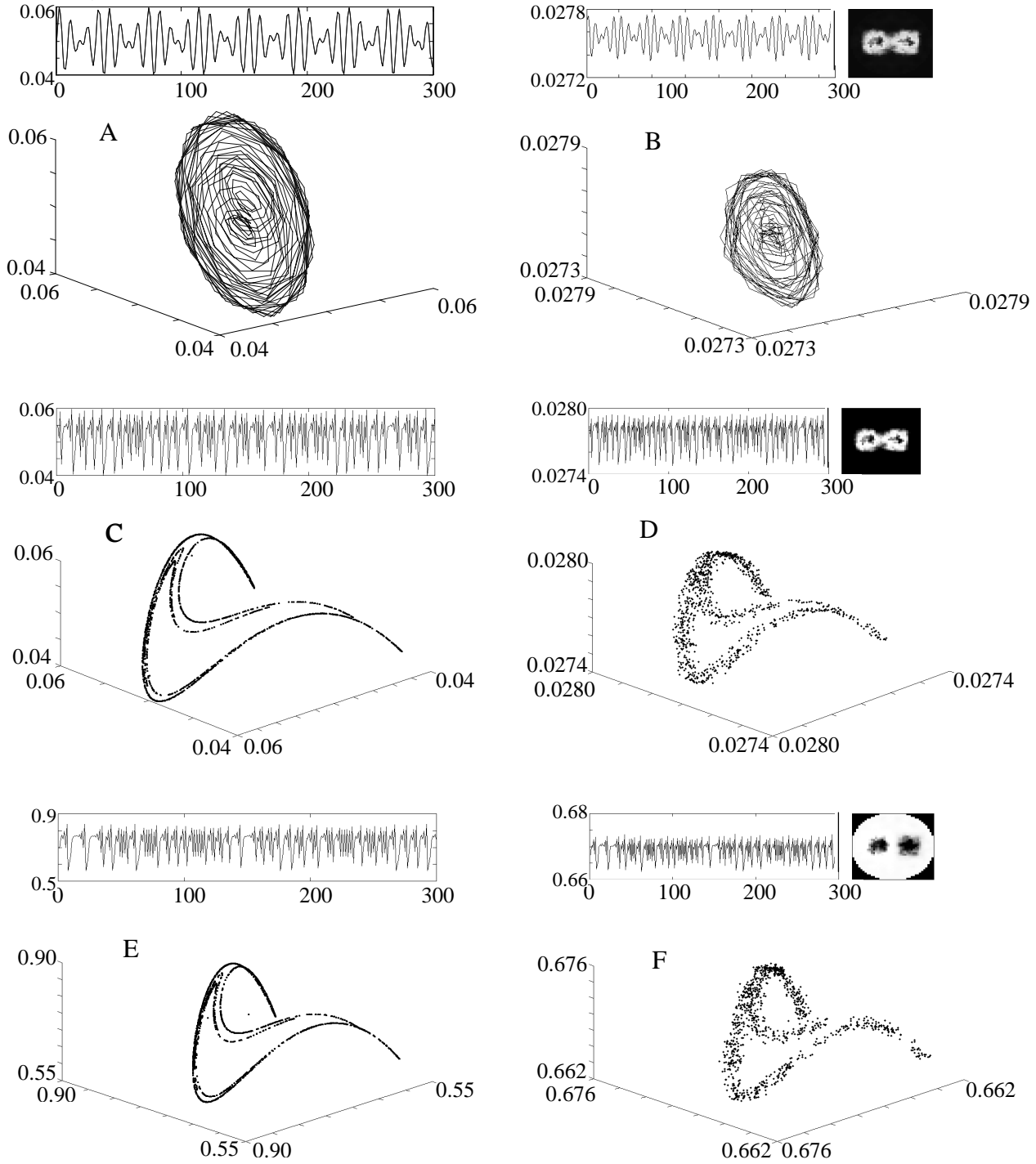
This can be simply demonstrated by computing a spatial map of the standard deviation of the image time series. This is shown in Figure 7. The principal difference between the results shown here and those in Figure 6 is the contrast level in the image. Because the background is static, its standard deviation is essentially zero, whereas the corresponding value in the

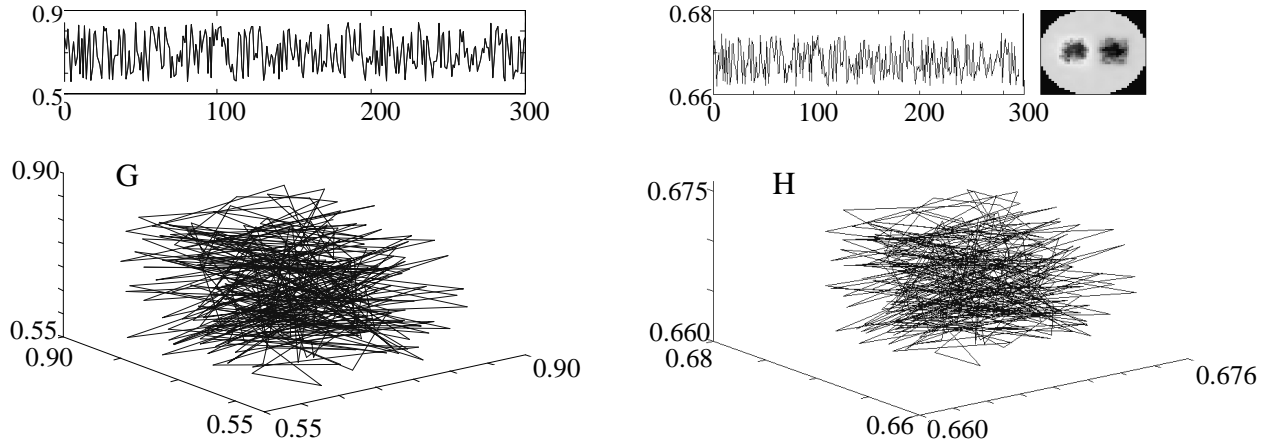


Legend Standard deviations of time series of V_b (Panel A) and of sO_2 (Panel B) of the dynamic target medium sketched in Figure 1.

inclusion is nonzero. While the observation of increased contrast is not surprising, it nevertheless directly shows that inclusions experiencing temporal variability can be identified with considerably improved quality. This leads to the more interesting question of just how well can spatially varying temporal behavior be defined. This is explored in the results shown in Figures 8–10

Figure 8





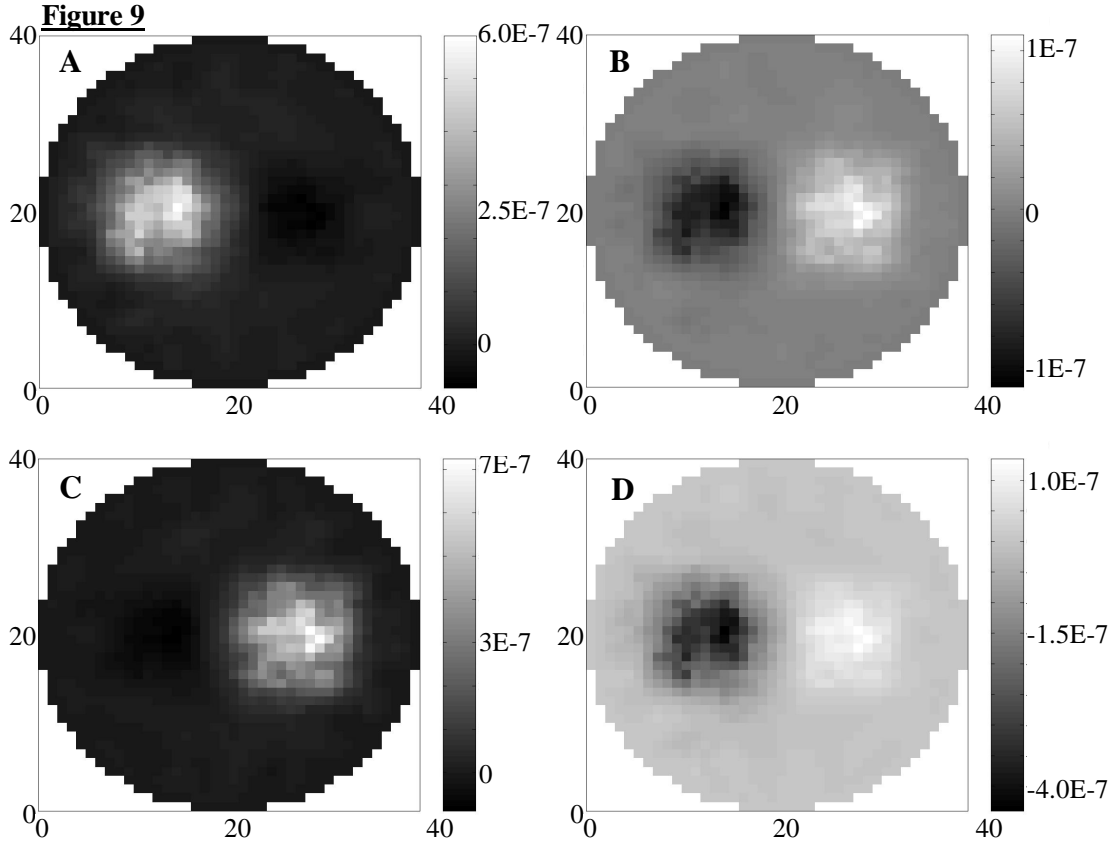
Legend Representative 3-D pseudo-state-space trajectories for modeled and reconstructed temporal variations in hemodynamic properties of the two inclusions in the nonlinear dynamics simulation study. Panel A, V_b modeled in left-hand inclusion (see Figure 1); panel B, reconstructed V_b time series in pixel (row=13,column=21); panel C, V_b modeled in right-hand inclusion; panel D, reconstructed V_b time series in pixel (27,21); panel E, sO_2 modeled in left-hand inclusion; panel F, reconstructed sO_2 time series in pixel (13,21); panel G, sO_2 modeled in right-hand inclusion; panel H, reconstructed sO_2 time series in pixel (27,21).

Recall from Methods, we have adopted a three-fold analysis scheme to define the accuracy with which temporal behavior is recovered and spatially mapped. A simple graphical means to assess accuracy is to compare the computed PSS attractors for the original and reconstructed time series. Figure 8 shows the dependence of this on the functional form of the time series introduced for the two hemodynamic properties. It will be recalled that in this study V_b and sO_2 fluctuated in time according to different mathematical functions at the same time and location. In Figures 8(A), (C), (E) and (G), we show the PSS representations ($m = 3$, $\tau = 1$) of the four modeled temporal fluctuations. Each of these is derived from one of the four functions plotted in Figure 2 (reproduced at the tops of the panels in Figure 8). Figures 8(B), (D), (E) and (H) show matching results from the time series of recovered $V_b(t)$ and $sO_2(t)$. The spatial map reproduced in the upper right portion of each panel is one particular image from the appropriate time series ($V_b(t)$ in Figures 8(B) and 8(D), $sO_2(t)$ in Figures 8(F) and 8(H)), while the curve plotted in the upper left portion is the recovered temporal variation in a single selected pixel (left-hand inclusion in Figures 8(B) and 8(F), right-hand inclusion in Figures 8(D) and 8(H)). The 3D PSS representation of the 2D curve also is shown in each Panel. It is seen that a markedly different form of PSS curve is obtained for each of the three qualitatively different types of modeled temporal variability, and that in every case the recovered function matches the modeled function closely.

While the results presented in Figure 8 demonstrate a strong positive correlation between the modeled and recovered temporal variability in the selected pixels, they do not directly address the practical questions of how accurately each of the four modeled hemodynamic functions is spatially localized in the $V_b(t)$ and $sO_2(t)$ maps and the degree of parameter cross-talk (*i.e.*, the magnitude by which one time series (*e.g.*, $V_b(t)$) overlaps with the another (*e.g.*, $sO_2(t)$)). The former can be determined by computing the covariance between the modeled and recovered function while the latter can be determined by comparing the time series of one recovered hemodynamic parameter to the time series used to model the other. Results of these computations are shown in Figures 9 and 10. Figures 9(A) and 9(C) are the computed covariance maps for $V_b(t)$. Inspection shows that the spatial maps of both the left and right hand inclusions correctly locate the position of the temporal behavior and nearly completely isolates one time-varying function from the other. A similar result is obtained for the $sO_2(t)$ maps (Figures 10(B) and 10(D)).

The degree of parameter cross-talk between the hemodynamic functions is revealed in the companion panels of Figure 9 and 10. Inspection of Figures 9(C) and 9(D) reveals that a fraction of the $sO_2(t)$ time series appears in the recovered $V_b(t)$ time series. The magnitude of cross-talk can be determined by comparing the maximum (absolute) value of covariance in Figure 9(A) or 9(C) to that in either 9(B) or 9(D). At first glance, this comparison suggests that the level of cross-talk is on the order of 15%. The true cross-talk level actually is much less. This is because covariance depends on the absolute amplitude of the varying functions, and these are not the same for the two modeled parameters. The variance in the modeled V_b time series is <1% that in the modeled sO_2 functions. After taking this difference into account, we find that the modeled $sO_2(t)$ accounts for <1% of the variability in the recovered $V_b(t)$ maps. A similar comparison involving the magnitude of cross-talk between the modeled $V_b(t)$ and recovered $sO_2(t)$ shows that, once again, we find that the level of cross talk is small (<1%).

Note that this seemingly reciprocal relationship is by no means guaranteed, because the forms of the functions used to derive the hemodynamic parameters from the reconstructed two-wavelength reconstructed image time series are qualitatively different.



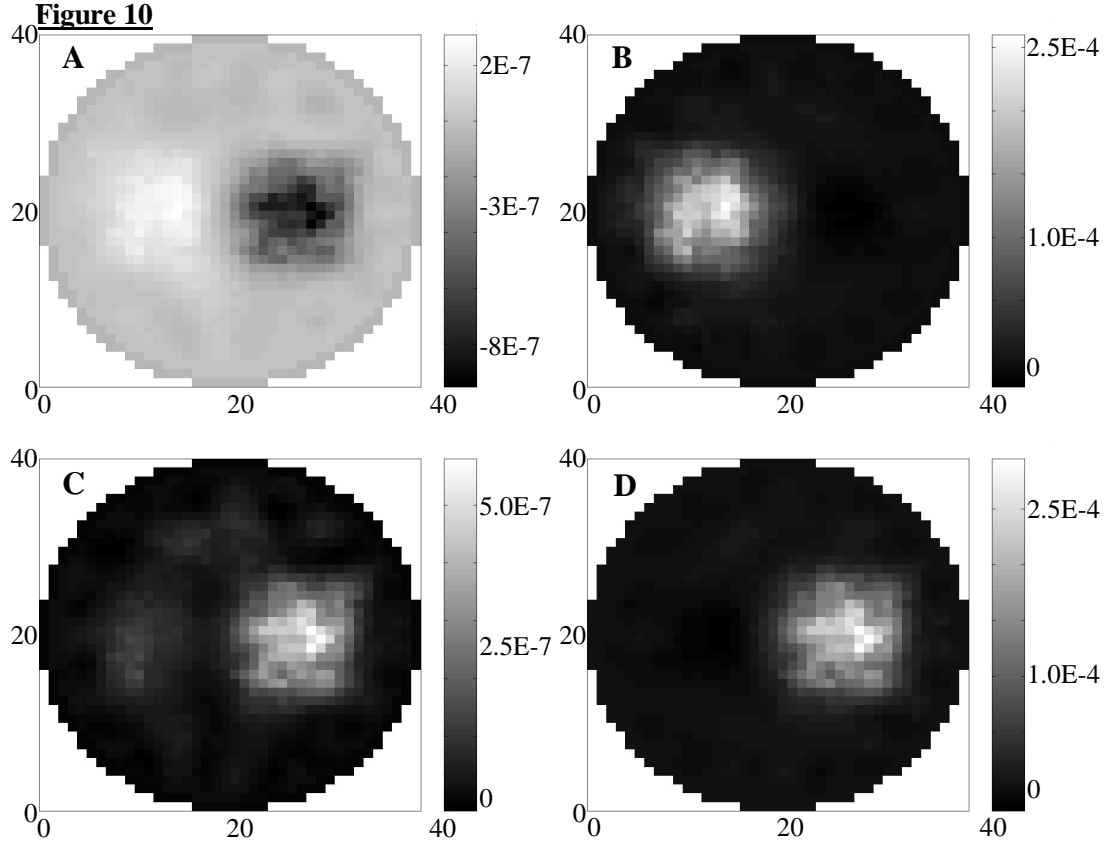
Legend Spatial maps of covariance between recovered $V_b(t)$ and the four simulated time-varying functions: (A) $V_b(l,t)$; (B) $sO_2(l,t)$; (C) $V_b(r,t)$; (D) $sO_2(r,t)$.

As a final measure of the accuracy with which the time-series image data were recovered, we have computed the value of the CD for each of the modeled functions for pixels lying with the actual boundary of the inclusions. These values are listed in Table 2 together with the expected values. Comparison shows that essentially in all cases, accurate recovery of the CD values were obtained.

4. DISCUSSION AND CONCLUSIONS

Characterization of functional processes often provides for the early detection of disease states. Because of the intimate relationship between tissue function and the vascular supply, measures of vascular dynamics may serve as windows into understanding not only the influence of disease processes, but also how tissues respond to the progression of the offending state. The availability of such measures could also serve as a guide to therapy. Drugs that influence tissue function, as many do, can be expected to provoke vascular responses. Characterization of the details of these responses could serve as a marker for identifying desirable or undesirable influences on the vasculature, as well as providing a measurable guide to improving dosing schedules.

Thus far, investigations of the temporal dynamics of blood flow in tissue have been restricted mainly to near-surface studies. Recently we have proposed that the method of dynamic optical tomography may be well suited to investigate vascular dynamics in large tissues.²⁴⁻²⁶ This capability arises from the observation that hemoglobin, which is nearly always restricted to the vascular space, is the principal absorber in tissue in the NIR region, and thus temporal variations in optical signal levels can be interpreted as originating principally from the time varying vascular response.



Legend Spatial maps of covariance between recovered $sO_2(t)$ and the four simulated time-varying functions: (A) $V_b(l,t)$; (B) $sO_2(l,t)$; (C) $V_b(r,t)$; (D) $sO_2(r,t)$.

Table 2 Correlation Dimensions for hemodynamics simulation

	$\nu(V_b)$		$\nu(sO_2)$	
	object	image	object	image
left inclusion	2	1.8 ± 0.06	1.21	1.3 ± 0.02
right inclusion	1.21	1.29 ± 0.025	3*	2.64 ± 0.08

Legend Computed values of the correlation dimension derived from the reconstructed image series. Symbols: ν , numerical value of the correlation dimension; V_b , tissue blood volume; sO_2 , blood oxygen saturation. (*) For stochastic fluctuations of the type used, ν is equal to the embedding dimension, which was 3 for this demonstration.

In this report we have provided preliminary evidence that the complex behavior of vascular dynamics can also be observed in cross section. In particular, we have found that the reconstructed time-series pixel data exhibits properties consistent with chaotic nonlinear behavior. We have further demonstrated that the same methods used to evaluate the physiological data are fully capable of accurately recovering and spatially mapping temporal behavior in the limiting case of spatiotemporal

coincident complex hemodynamic states. Currently underway are studies seeking to define the spatiotemporal dynamics of the vascular response of breasts with neoplastic disease, and evoked-response studies on adult brain.

5. ACKNOWLEDGMENT

This research was supported by NIH grant RO1-CA 66184.

6. REFERENCES

1. C. H. Schmitz, M. Löcker, J. Lasker, A. H. Hielscher, and R. L. Barbour, "Performance characteristics of a silicon photodiode (SiPD) based instrument for fast functional optical tomography," Proc. SPIE Vol. 4250 (2001, accompanying report).
2. Y. Pei, H. L. Graber, and R. L. Barbour, "Method for minimizing inter-parameter cross-talk in reconstructed images of spatially heterogeneous scattering and absorption coefficients," Proc. SPIE Vol. 4250 (2001, accompanying report).
3. L. Glass and M. C. Mackey, *From Clocks to Chaos: The Rhythms of Life* (Princeton University Press, Princeton, NJ 1998).
4. H. L. Graber, Y. Pei and R. L. Barbour, "Imaging of spatiotemporal coincident states by dynamic optical tomography," Proc. SPIE 4250 (2001, accompanying report).
5. G. Landis, S. Blattman, T. Panetta, C. H. Schmitz, H. L. Graber, Y. Pei, and R. L. Barbour, "Clinical applications of dynamic optical tomography in vascular disease," Proc. SPIE 4250 (2001, accompanying report).
6. G. Nuzacci, A. Evangelisti, D. Righi, G. Giannico, and I. Nuzacci, "Is there any relationship between cold-induced vasodilation and vasomotion?" *Microvascular Research* **37**, 1-7 (1999).
7. C. H. Schmitz, H. L. Graber, H. Luo, I. Arif, J. Hira, Yaling Pei, A. Bluestone, S. Zhong, R. Andronica, I. Soller, N. Ramirez, S.-L. S. Barbour, R. L. Barbour, "Instrumentation and calibration protocol for imaging dynamic features in dense-scattering media by optical tomography," *Applied Optics* **39**, 6466-6486 (2000).
8. B. J. Tromberg, O. Coquoz, J. B. Fishkin, T. Pham, E. R. Anderson, J. Butler, M. Cahn, J. D. Gross, V. Venugopalan, and D. Pham, "Non-invasive measurements of breast tissue optical properties using frequency-domain photon migration," *Philosophical Transactions of the Royal Society of London B* **352** 661-668 (1997).
9. A. H. Nayfeh and B. Balachandran, *Applied Nonlinear Dynamics: Analytical, Computational, and Experimental Methods* (John Wiley & Sons, New York, 1995), Chap. 4.
10. K. Briggs, "An improved method for estimating Liapunov exponents of chaotic time series," *Physics Letters A* **151**, 27-32 (1990).
11. B. Chance, S. Nioka, J. Kent, K. McCully, M. Fountain, R. Greenfeld, and G. Holtom, "Time-resolved spectroscopy of hemoglobin and myoglobin in resting and ischemic muscle," *Analytical Biochemistry* **174**, 698-707 (1988).
12. T. E. J. Gayeski, R. J. Connett, and C. R. Honig, "Minimum intracellular P_{O_2} for maximum cytochrome turnover in red muscle in situ," *American J. Physiology* **252**, H906-H915 (1987).
13. O. W. van Assendelft, *Spectrophotometry of Haemoglobin Derivatives* (Charles C. Thomas, Springfield, IL, 1970).
14. Y. Pei, "Optical Tomographic Imaging Using Finite Element Method," Ph.D. Dissertation, Polytechnic University, Brooklyn, NY, 1999.
15. P. Grassberger and I. Procaccia, "Characterization of strange attractors," *Physical Review Letters* **50**, 346-349 (1983).
16. M. T. Rosenstein, J. J. Collins, and C. J. de Luca, "A practical method for calculating largest Lyapunov exponents from small data sets," *Physica D* **65**, 117-134 (1993).
17. T. M. Griffith, "Temporal chaos in the microcirculation," *Cardiovascular Research* **31**, 342-358 (1996).
18. Ref. 9, Chap. 7.
19. W. L. Ditto, M. L. Spano, H. T. Savage, S. N. Rauseo, J. Heagy, and E. Ott, "Experimental observation of a strange nonchaotic attractor," *Physical Review Letters* **65**, 533-536 (1990).
20. U. Parlitz, "Identification of true and spurious Lyapunov exponents from time series," *Int. J. Bifurcations and Chaos* **2**, 155-165 (1992).
21. P. Grassberger and I. Procaccia, "Measuring the strangeness of strange attractors," *Physica D* **9**, 189-208 (1983).
22. J. Theiler, "Spurious dimension from correlation algorithms applied to limited time-series data," *Physical Review A* **3**, 2427-2432 (1986).
23. D. Prichard and J. Theiler, "Generating surrogate data for time series with several simultaneously measured variables," *Physical Review Letters* **73**, 951-954 (1994).
24. R. L. Barbour, H. L. Graber, C. H. Schmitz, Y. Pei, S. Zhong, S.-L. S. Barbour, S. Blattman, and T. Panetta, "Spatiotemporal imaging of vascular reactivity by optical tomography," *Proceedings of Inter-Institute Workshop on In Vivo Optical Imaging at the NIH*, A. H. Gandjbakhche, Ed. (Optical Society of America, Washington, DC 2000), pp. 161-166. (Presented at the National Institutes of Health, Bethesda, MD, Sept. 16-17, 1999.)

25. H. L. Graber, C. H. Schmitz, Y. Pei, S. Zhong, S.-L. S. Barbour, S. Blattman, T. Panetta, R. L. Barbour, "Spatio-Temporal Imaging of Vascular Reactivity," in *Medical Imaging 2000: Physiology and Function from Multidimensional Images*, C.-T. Chen, A. V. Clough, Eds., Proceedings of SPIE Vol. 3978, pp. 364–376 (2000).
26. R. L. Barbour, H. L. Graber, Y. Pei, S. Zhong, and C. H. Schmitz, "Optical tomographic imaging of dynamic features of dense-scattering media," *J. Opt. Soc. Am. A* (2001), in press.